
# Spectrum Compact CE System

## Sanger sequencing and fragment/STR analysis

- benchtop 4-capillary electrophoresis instrument compatible with 4-, 5- and 6-dye chemistries
- processes up to 32 samples in a single run and is compatible with most commercially available kits
- flexible raw data analysis, even with already available versions of analysis software
- prefilled, plug-and-play consumables offer maximal flexibility and resource efficiency
- controlled by the integrated touchscreen or by Remote Access Software
- on-site instrument and software installation, operational and application trainings

www.promega.com/spectrum-compact-system

Spectrum COMPACT CE SYSTEM

**Maika Felten**[1]
**Wolfgang Staroske**[2]
**Magnus S. Jaeger**[1]
**Petra Schwille**[2]
**Claus Duschl**[3]

[1]Department of Biotechnology and Medical Technology, Saarland University Hospital, Homburg/Saar, Germany
[2]Biotechnology Centre, Technische Universität Dresden, Dresden, Germany
[3]Fraunhofer Institute for Biomedical Engineering (IBMT), Potsdam, Germany

Received November 21, 2007
Revised February 22, 2008
Accepted February 25, 2008

Research Article

# Accumulation and filtering of nanoparticles in microchannels using electrohydrodynamically induced vortical flows

We present an approach for the accumulation and filtering of nano- and microparticles in microfluidic devices that is based on the generation of electric traveling waves in the radio-frequency range. Upon application of the electric field *via* a microelectrode array, complex particle trajectories and particle accumulation are observed in well-defined regions in a microchannel. Through the quantitative mapping of the 3-D flow pattern using two-focus fluorescence cross-correlation spectroscopy, two vortices could be identified as one of the sources of the force field that induces the formation of particle clouds. Dielectrophoretic forces that directly act on the particles are the second source of the force field. A thorough 2-D finite element analysis identifies the electric traveling wave mechanism as the cause for the unexpected flow behavior observed. Based on these findings, strategies are discussed, first, for avoiding the vortices to optimize electrohydrodynamic micropumps and, secondly, for utilizing the vortices in the development of microdevices for efficient particle accumulation, separation, and filtering. Such devices may find numerous biomedical applications when highly diluted nano- and microsuspensions have to be processed.

**Keywords:**
Dielectrophoresis / Fluorescence correlation spectroscopy / Lab-on-chip / Microfluidics / Traveling electric waves DOI 10.1002/elps.200700844

## 1 Introduction

In biology, chemistry, and medicine, the processing of micro- and nanoparticles in a continuous flow is a key requirement in an increasing number of applications ranging from the detection of pathogens to the purification of samples [1]. One option to handle particles suspended in liquids is to use electric, magnetic, or acoustic fields [2–4]. The forces generated through these fields typically scale with the volume of the suspended objects ($\propto r^3$). Hence, for the manipulation of sub-micrometer objects, either unreasonably high field strengths that are often not compatible with sensitive biological samples or schemes that depend on passive diffusion of particles are necessary [5]. The latter approach requires a reduction of dimensions, which limits throughput. Another option for the processing of particles in microchannels depends on the generation of hydrodynamic forces. However, it is difficult to create defined turbulent flow patterns in microchannels where normally laminar flow prevails, characterized by low Reynolds numbers. Electrothermally induced flow is an interesting method to collect and trap bioparticles based on the generation of vortices [6–8]. In this regime, the fluid flow is electroosmotically driven through the motion of charges of the electric double layer on the surface of the electrodes. However, the efficiency of vortex formation scales with the surface area of the electrode. In addition, electroosmosis requires relatively high voltages and low frequencies. Both effects easily evoke electrochemical degradation of sensitive biological samples or of the electrodes.

In the past, several approaches demonstrated that electrohydrodynamic pumping is suited for the transport of liquid media in microfluidic devices [9–11]. The pumping mechanism is based on the generation of electric traveling waves in the radio frequency range using arrays of microelectrodes. Recently, we characterized the performance of such a micropumping device by measuring the net flow of microparticles distant from the electrode array as a function of the temperature field in the fluid medium [9]. In these regions of the channel where no electrodes were present, the flow was laminar and characterized by low Reynolds num-

**Correspondence**: Dr. Magnus Jaeger, c/o Fraunhofer-IBMT, Am Muehlenberg 13, D-14476 Potsdam, Germany
**E-mail**: m.jaeger@mx.uni-saarland.de
**Fax**: +49-331-581-87-399

**Abbreviations**: **2f-FCCS**, two-focus fluorescence cross-correlation spectroscopy; **AC**, auto-correlation; **APD**, avalanche photodiode; **DEP**, dielectrophoresis; **FCC**, flow cross-correlation; **FCS**, fluorescence correlation spectroscopy

bers and a conventional Poiseuille profile. However, we observed a complex behavior of the microparticle trajectories in the region above the microelectrodes. In well-defined regions of the channel, particle agglomeration occurred that, in part, seemed to be caused by a turbulent flow pattern of high stability.

Here, we investigate the force field induced by the traveling wave mechanism that determines the complex flow and the unexpected particle trajectories for two reasons: first, understanding the turbulent flow pattern may help optimize the performance of the micropumps. Secondly, these flow patterns in combination with dielectrophoretic (DEP) effects allow the accumulation and filtering of particles. In this contribution, however, 7we focus on the second point with special emphasis on the exploration of its potential for technological applications. The trapping and filtering effect is demonstrated for two different sizes of particles. To elucidate the mechanism, a quantitative investigation of the induced flow pattern is performed. Using tracer beads with sizes that can be tracked visually is inapplicable to the detection of the flow velocity. This is due to the applied field also inducing non-negligible DEP forces on such particles as these forces scale with the volume of the particles ($\propto r^3$). We employed two-focus fluorescence cross-correlation spectroscopy (2f-FCCS) to map the 3-D flow in the microchannel. In fluorescence correlation spectroscopy (FCS), the motion of dye-labeled particles is analyzed in an open confocal volume [12–16]. FCS is not only used to measure free 3-D diffusion but also to characterize directed motion associated with flow or active transport [17, 18]. Standard FCS employs only one focal volume. In this mode, flow velocities can only be measured when the transit time through the confocal volume due to flow is much shorter than the transit time due to free diffusion. As pointed out above, in our case, the option of slowing down the diffusive motion by increasing the size of the fluorescent probes is limited. Therefore, 2f-FCCS was employed [19, 20]. The distance between the two foci is an additional ruler, which allows to separate between flow and diffusion and provides direction-dependent information at the same time.

With a thorough 2-D finite element analysis, the causes of the main features of the obtained flow pattern can be identified. By adding the action of DEP forces, an almost complete explanation of the observed phenomena can be given.

## 2 Materials and methods

### 2.1 Fabrication and actuation of the micropump

The manufacturing of the microstructures is based on well-established photolithographical techniques [21]. The device consists of two glass plates separated by a polymer spacer (SU-8) that includes the microfluidic channel (see Fig. 1). The channel is 40 μm high, 200 μm wide and 14 mm long. For ensuring the fluidic access, holes are drilled into one of the glass plates before assembly of the chip. The integrated pumping unit is composed of 36 platinum electrodes forming a planar array with a total length of 710 μm on the channel bottom. As an adhesion layer, titanium is used. To minimize electric losses at the supply lines, the electrodes are passivated outside the channel region by a silicon nitride layer. The electrodes are 200 nm thick and their width as well as the gap between them is 10 μm. The electrodes are energized (Cytocon 400 generator with 32 channels, Evotec Technologies, Hamburg, Germany) using four rectangular AC signals of voltages between 5 and 10 V and radio frequencies (1 to 10 MHz). Phase shifts between the signals applied to next-neighbor electrodes are $\pi/2$ (see Fig. 1), resulting in a traveling electric potential wave at the electrode layer. The signal output of the generator was monitored using a

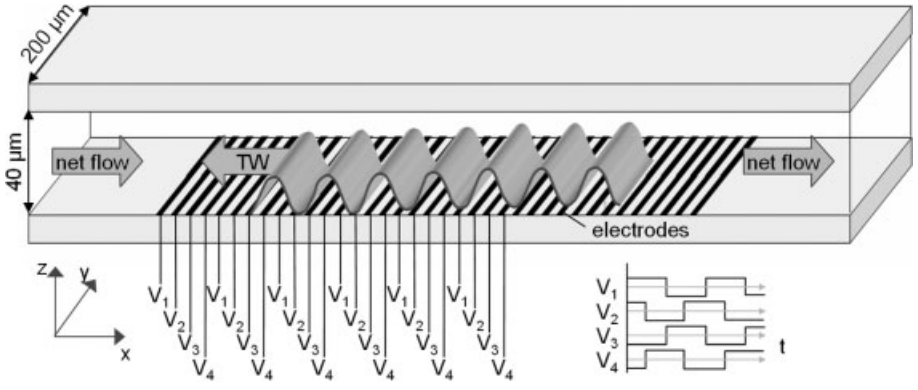


**Figure 1.** Detail sketch of a of the microfluidic channel containing a traveling wave micropump. The total channel length is 14 mm of which the electrode array occupies 710 μm. The device consists of two glass plates separated by a 40-μm thick polymer spacer. The electrodes are energized using four rectangular signals. This results in a potential wave traveling to the left along the electrode layer. Ohmic heating leads to gradients in the conductivity and permittivity. Thus, volume charges are induced which interact with the electric field such that a longitudinal net flow opposite to the travel direction of the potential wave occurs.

 

four-channel digital oscilloscope (TDS3034B, Tektronix). The fluidic channel is filled with aqueous solutions of different electric conductivities (10 to 70 mS/m) that are adjusted by adding NaCl. Fluorescent polystyrene particles of different sizes (200 nm, 1 μm, Polysciences Europe, Germany) are suspended in the solution.

### 2.2 Simulations

The electric force profile along the *z*-axis and the temperature distribution in the microchannel geometry (see Fig. 2) were calculated by 2-D finite element analysis using a partial differential equation solver (FlexPDE 2.22, FlexPDE solu-

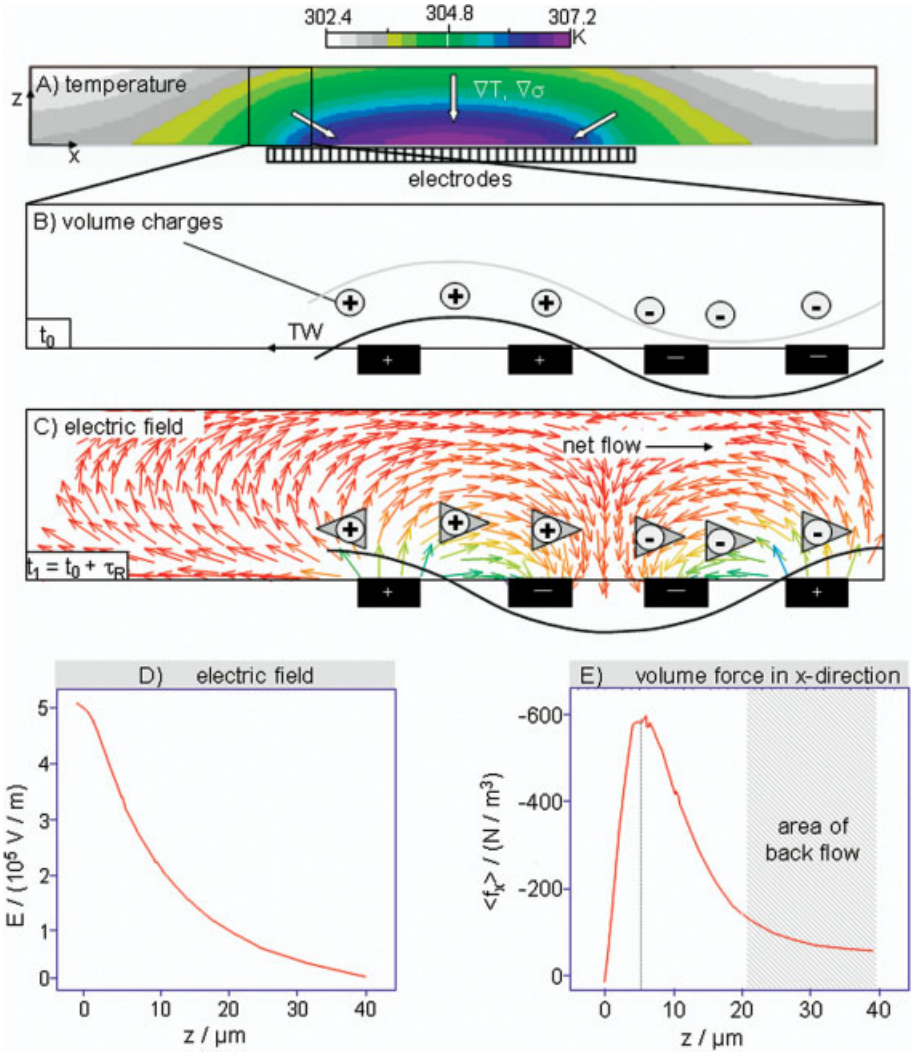


**Figure 2.** Representation of the results of the simulation using finite element analysis. Exposing a liquid to an electric traveling wave results in Ohmic heating of the liquid. The contour plot in (A) shows the temperature distribution in the channel. Since the electric conductivity $\sigma$ and the permittivity $\varepsilon$ of the liquid are functions of the temperature, the temperature gradient is accompanied by the gradients $\nabla\sigma$ and $\nabla\varepsilon$. In combination with the electric field, these gradients give rise to the formation of volume charges in the liquid bulk as shown in (B). The charge distribution in the liquid (gray curve) mirrors the potential distribution at the electrodes (black curve) at $t_0$. After the potential wave has propagated along the electrodes for the relaxation time $\tau_R \approx \pi/4$, the electric field distribution corresponds to that shown in (C). The color value of the arrows indicates the strength of the electric field. The triangles around the charges point into the *x*-direction of the acting force. All triangles but the leftmost are aligned in the same direction indicating the concerted action of the force field. A net flow of the fluid is induced. Due to the field distribution at the boundary of the array, volume element forces opposite to the net flow are induced in this region. The electric parameters in the calculations are equal to those used for the 2f-FCCS measurement in Fig. 4. The external temperature was 300 K. (D) The graph shows the electric field strength as a function of the *z*-coordinate along a line between two oppositely charged electrodes, where the field polarization is purely longitudinal (*e.g.* between the first and second electrode from the left, C). (E) The *z*-scan of the electric force density. The location of the maximum of the electric force ($\approx$ 6 μm) coincides with the position of maximum flow derived from the 2f-FCCS measurement ($\approx$ 10 μm). The area where backflow is observed is marked in the diagram. In this region, the volume force has decreased by a factor of ten. There, the force impeding a liquid motion opposite to the net flow direction is low.

 

tions). In this approach, the appropriate choice of the boundary conditions is crucial. In particular, the heat dissipation through the glass plates forming the channel walls was included. Further details of the boundary conditions are found elsewhere [22].

### 2.3 Flow detection using 2f-FCCS and visual tracking

The 2f-FCCS measurements were performed on a home-made setup (Fig. 3A). As fluorescent species, we used CdSe/ZnS quantum dots (Adirondack Green, Evident Technologies, Troy, NY) with a size of 20 nm at a concentration of 100 nM. On the one hand, the size of the particles was chosen to be big enough so that motion due to diffusion did not interfere with directed flow. On the other hand, particles had to be small enough not to be affected by DEP. For excitation of the quantum dots, the laser line at 488 nm from an Ar-Kr laser (Inova 70, Coherent) was used. The laser beam was split and recollected by two beam splitters, so that the two beams entered the objective (UPlanApo 60 x/1.2 W, Olympus, Hamburg, Germany) with a small angle difference. They created two foci separated by a distance of 2.2 μm. Each focus was 3.3 μm high, 560 nm wide and had an effective volume of 0.73 fL. The fluorescence light emitted from the quantum dots ($\lambda$ = 520 nm) was separated from the excitation light by a dichroic beam splitter (Q 505 LP, AHF, Tuebingen, Germany) and filtered by an emission filter (HQ 532/70, AHF). The fluorescence light from both foci was focused onto the one-end side of a double-core multi-mode Y-fiber which splits into two fibers containing one core each, a so-called bifurcated fiber (Avantes, RB Eerbeek, The Netherlands) and was detected with an avalanche photodiode (APD) (SPCM-CD 3017, Perkin Elmer). The signals from the APD were processed to obtain an auto-correlation curve from each spot and two cross-correlation curves, one in backward and one in forward direction, using a hardware correlator (Flex02-12D/B, Correlator, Bridgewater, NJ). At each position in the microchannel, we measured the fluorescent signals six times over a period of 60 s. The correlation curves were evaluated with a Matlab script (The Mathworks, Natick, MA). For the evaluation of the flow velocity, the backward cross-correlation curve was subtracted from the forward cross-correlation curve, leading to the flow cross-correlation (FCC) curve, without any spatial crosstalk as described by Brinkmeier *et al.* [19]. The FCC curve and the auto-correlation (AC) curves were fitted globally based on Eqs. (2) and (3), using weighted residuals. The residuals of the FCC were weighted five times higher than the residuals of the AC.

In the flow measurement experiments, we used an aqueous solution with a conductivity of 35 mS/m. The driving voltage was 8 V and the frequency 7 MHz.

For the visual tracking of particle trajectories, an Olympus IX71 inverted microscope (Olympus) in a standard fluorescence configuration was used. For image recording, a

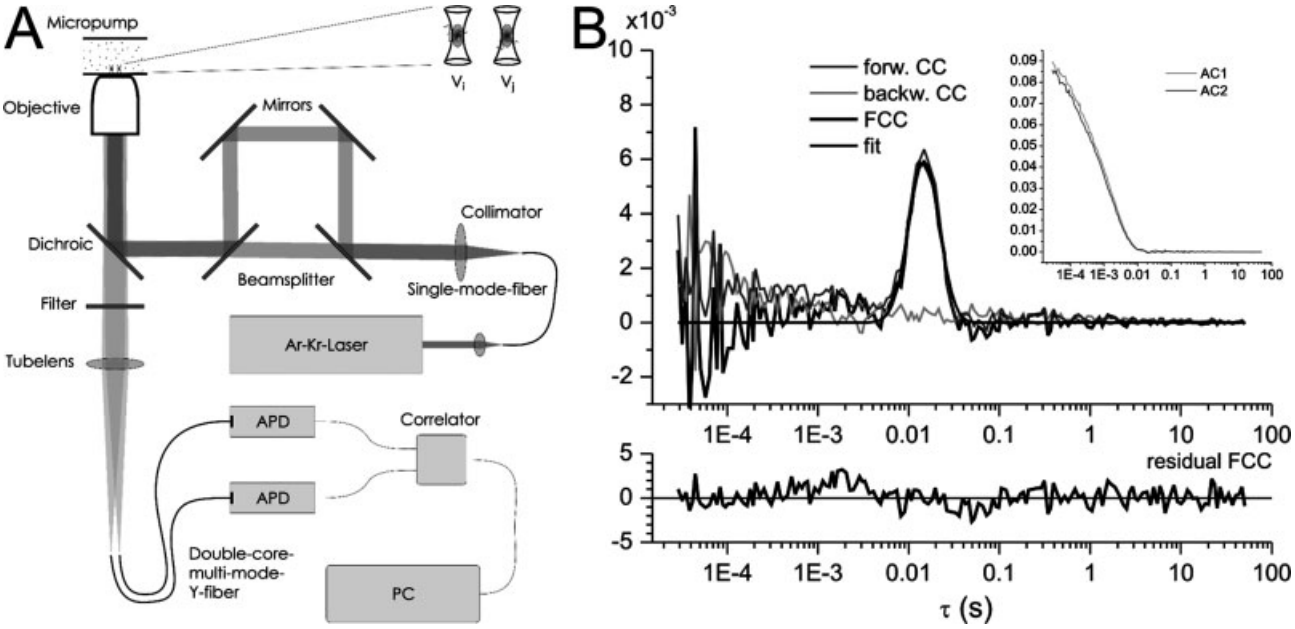


**Figure 3.** (A) Home-made 2f-FCCS setup. Two laser beams enter the objective under a small angle, creating two laser spots inside the microchannel. The emitted fluorescence light is collected by the same objective, directed onto a double-core multi-mode Y-fiber and detected with two APD. The signals from the APD are correlated with a hardware correlator and evaluated on a PC. (B) Correlation curves measured at position $x$ = 280 μm, $y$ = 100 μm, $z$ = 10 μm. In addition to the measured forward and backward cross-correlation, the FCC curve is shown which is calculated by subtraction of the backward from the forward cross-correlation. The AC curves are shown in the inset. The FCC curve was fitted and gives a flow velocity of 126 μm/s. The weighted residuals from the fit are shown in the lower graph.

 

CCD camera (Orca ER, Hamamatsu, Germany) was employed in a constant frame rate mode. Only particles that remained in the focal plane of the microscope for a sufficient period were used for the determination of their velocity. Data were processed if required using the image analysis software "Image-Pro Plus 4.0" from Media Cybernetics.

### 2.4 Theory

#### 2.4.1 Traveling wave pumping mechanism

The propagation of the electric field is achieved through the application of phase-shifted signals to neighboring electrodes. The field induces polarization charges in the fluid if gradients of the electric conductivity and/or dielectric properties are present perpendicular to the plane of the array. Such gradients are generated through an uneven temperature distribution in the fluid. For example, local Ohmic heating through the applied electric field may be the source for such a temperature field. If the frequency of the wave is such that a phase shift of $\pi/4$ equals the relaxation time $\tau_R$ of the polarization charges, then the lateral component of the electric field optimally acts on the charges and produces the maximum net flow. The electrode arrays are compatible with lithographic methods and can be integrated into microfluidic devices.

Exposing a dielectric liquid to a propagating electric field may lead to the motion of the liquid. For an incompressible liquid, the electric volume force $\mathbf{f}_{el}$ can be expressed by [23]:

$$\vec{\mathbf{f}}_{el} = \rho\vec{\mathbf{E}} - \frac{1}{2}E^2\nabla\varepsilon \quad (1)$$

where $\rho$ is the volume charge density, $\mathbf{E}$ is the electric field, and $\varepsilon$ is the permittivity of the medium. This equation makes obvious that either free volume charges or polarization charges are necessary to obtain a net force through an electric field. In the present work, these charges are generated through a high-frequency traveling electric potential wave in the liquid using an array of linear electrodes (see Fig. 1). For such a configuration, the time-averaged electric force density can be derived from Eq. (1) if the applied electric field follows $\vec{\mathbf{E}}(t) = \vec{\mathbf{E}}_0 e^{i\omega t}$ and oscillates with an angular frequency $\omega$ [24]. The electric force density is a function of the electric conductivity $\sigma$ as a result of considering all relevant contributions of $\rho$ in Eq. (1). Gradients of $\sigma$ and $\varepsilon$ of the fluid are required to obtain a pumping effect.

For calculating the potential distribution $\phi$ and, thus, the electric field in the microchannel, the Laplace equation was solved [22].

The electric field also causes highly localized Ohmic heating that gives rise to the generation of gradients in $\sigma$ and $\varepsilon$. To determine the temperature profile in the fluid, the energy balance equation has to be solved [25]. It balances the thermal conductivity $k_t$ and the time-averaged power generation through the electric field. The warming is localized near the electrodes and, hence, produces a temperature gradient pointing towards the electrode plane [9]. As the electric conductivity $\sigma = \sigma(T)$ and the permittivity $\varepsilon = \varepsilon(T)$ of the liquid are functions of temperature, gradients in these electric properties occur [26].

In summary, the component of the electric field parallel to the gradients $\nabla\sigma$, $\nabla\varepsilon$ induces charges whereas the longitudinal component exerts a force on these charges while both components produce the temperature profile. To obtain a net flow of the liquid, the forces have to act in a coherent and unidirectional manner on the volume elements of the fluid. This is the case when the frequency of the field and the relaxation time $\tau_R$ of the polarization charges correspond to each other. In order to exert a maximum flow, the phase lag between the distribution of the polarization charges induced by the propagating field at $t_0$ and the field distribution at $t_1 = t_0 + \tau_R$ must be $\pi/4$ (see Fig. 2C).

#### 2.4.2 Flow detection using 2f-FCCS

The velocity distribution in the microchannels was measured using 2f-FCCS. The model for 2f-FCCS was first derived by Brinkmeier *et al.* [19]: the fluctuations $\delta F_{i,j}(t)$ of the fluorescence signals $F_{i,j}(t)$ predominantly arise from quantum dots, which diffuse in and out of the respective focal volumes $V_i$ and $V_j$. They are proportional to the fluctuations of the concentrations $\delta C_{i,j}(t)$. The AC (Eq. 2) and FCC (Eq. 3) functions are obtained by, firstly introducing the shape of the focal volumes and, secondly, adding the travel distance $v\tau$ representing the flow to the standard 3-D diffusion:

$$G_{AC}(\tau) = \frac{1}{CV_{eff}} \cdot \frac{1}{1+\frac{4D\tau}{\omega_0^2}} \cdot \frac{1}{\sqrt{1+\frac{4D\tau}{z_0^2}}} \cdot \exp\left(-\frac{v^2\tau^2}{\omega_0^2+4D\tau}\right) \quad (2)$$

$$G_{FCC}(\tau) = \frac{1}{CV_{eff}} \cdot \frac{1}{1+\frac{4D\tau}{\omega_0^2}} \cdot \frac{1}{\sqrt{1+\frac{4D\tau}{z_0^2}}} \cdot \exp\left(-\frac{v^2\tau^2+R^2-2Rv\tau\cos\alpha}{\omega_0^2+4D\tau}\right) \quad (3)$$

where $D$ is the diffusion constant, $\tau$ the lag time, $V_{eff}$ the effective detection volume, $R$ the lateral distance between both foci and $\alpha$ the angle between a line connecting the two foci and the flow direction. The $\omega_0$ is the radius perpendicular to, and $2z_0$ the length along, the optical axis of the focal detection volume.

## 3 Results

### 3.1 Characterization of the particle enrichment

Electrohydrodynamic pumps transport liquid media in microfluidic devices. The flow of microparticles distant from the electrode array is characterized by a Poiseuille profile [9]. However, we observed a complex behavior of the trajectories of microparticles above the microelectrodes. During traveling wave pumping, particles accumulated and were filtered at some positions above the electrodes. Particle agglomeration

 

occurred in well-defined regions of the channel. These phenomena are not observed in other regions in the channel, where no electrodes are present. We investigated the parameters that are crucial for the complex flow dynamics observed.

Figure 4 shows four micrographs that document the sampling of fluorescent polystyrene particles with sizes of 200 nm and 1 μm, respectively, caused by the action of a traveling electric field in one of the microchannels fabricated. Within a few minutes, bright patches developed at defined positions on top of the electrode array (black lines). The agglomeration regions of 1 μm-sized particles were much more confined than those formed by the 200-nm particles. However, in both cases, the brightest regions were found between the third and seventh electrode from the left. This was also observed for other particle suspensions. Even for a particle size of 50 nm, a slight increase of the fluorescent signal above the electrodes was observed. The temporal development of the fluorescence intensity due to the enrichment of 200 nm-sized particles is shown in Fig. 4C and is consistent with a steady influx of particles from the left side. The filtering efficiency for 1 μm-sized particles is close to 100% [the spots on the right side of image 4A (right) stem from immobile particles]. The efficiency for 200-nm particles was more difficult to analyze due to the fluorescence background but was estimated to be at least 90%. The formation of particle patches shows a robust behavior against moderate variations not only of the particle size but also of the voltage, the ionic strength of the aqueous solution, and of the channel and the array geometry. For example, a change of the applied voltage (1 $V_{rms}$ to 10 $V_{rms}$) or a variation of the electric conductivity of the liquid (0.1 to 100 mS/m) do not alter the qualitative behavior of the process. Similarly, we have tested ring-like channels and channels equipped with curved electrode geometries that produced the same flow pattern.

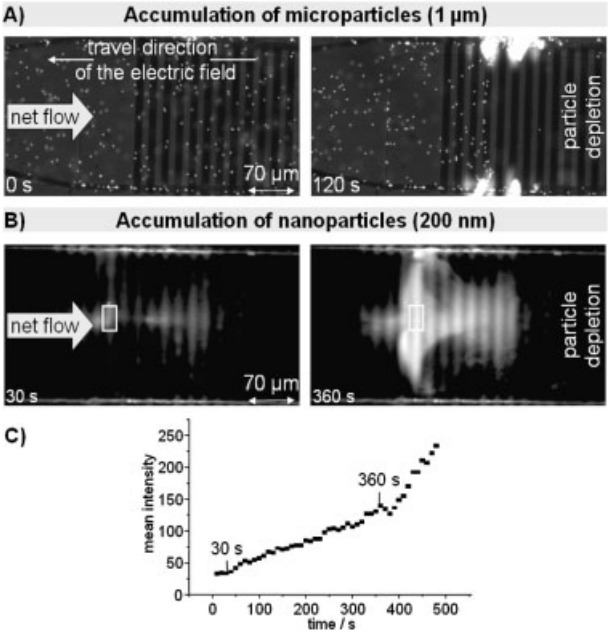


**Figure 4.** Trapping of (A) 1 μm and (B) 200 nm fluorescent particles. The left images show the situation at the beginning of the experiment. After the traveling wave pump is switched on, a rightward net flow transports the particles to the electrode region. The combination of hydrodynamic and DEP forces leads to a trapping of particles. Parameter sets: (A) 10 mS/m, 6.25 MHz, 4 V and (B) 67 mS/m, 10 MHz, 4.5 V. (C) Time course of the fluorescence intensity increase that reflects the accumulation of 200-nm particles. The values result from the averaging of the intensity over the area sketched in the micrograph in (B).

### 3.2 Measurement of the velocity profile using 2f-FCCS

The flow distant from the electrode array can be detected by using tracer beads in the μm size range and shows a laminar Poiseuille flow profile [9]. Above the electrodes, the motion of such tracer beads cannot be attributed to hydrodynamic drag forces only but is also affected by DEP forces acting directly on the particles. The action of these forces can be separated through 2f-FCCS, as it allows employing particles of much smaller size. As tracers, we used semiconductor particles with a diameter of 20 nm. The 2f-FCCS enabled us to derive the motion of the tracers from the cross-correlation of the fluorescent signals produced in two foci (Eq. 3). Typical correlations obtained from the 2f-FCCS measurements are shown in Fig. 3B. By fitting Eq. (3) to the FCC curve, the flow velocity was derived. To map the velocity profile in the part of the microchannel where the electrode array is located, the position of the two foci was systematically scanned through the channel volume. Figure 5 summarizes the results from all 2f-FCCS measurements. The graphs represent scans along three mutually perpendicular axes above the electrode array. Positive velocity values indicate flow in the same direction as the net flow in those regions of the channel where no electrode is present. The $x$-scan was detected 10 μm above the electrode plane at half of the channel width. Above the left part of the electrode array, the flow runs opposite to the direction of the net flow (Fig. 5A). For $x$-values larger than 200 μm, *i.e.* behind the tenth electrode, the flow direction reverses and coincides with the net flow direction. Between 500 and 700 μm, the flow is fastest and reaches velocities of up to 300 μm/s. This is approximately six times the maximum flow velocity of the Poiseuille flow outside the electrode array (line in Fig. 5A). The $y$-scan was also measured 10 μm above the electrodes at $x = 600$ μm (Fig. 5B). The distribution of measured flow velocities is well approximated by a parabolic profile. Along the $z$-direction, a reversal of the flow is observed for larger $z$-values (Fig. 5C). Here, the zero-crossing point is located in the middle of the channel. However, the flow showing a positive sign and being closer to the electrodes is approximately two times faster than the backflow observed near the channel top. Consequently, more liquid is transported along the positive $x$-direction than in the opposite direction. This pattern is compatible with the positive net flow. Figure 6

 

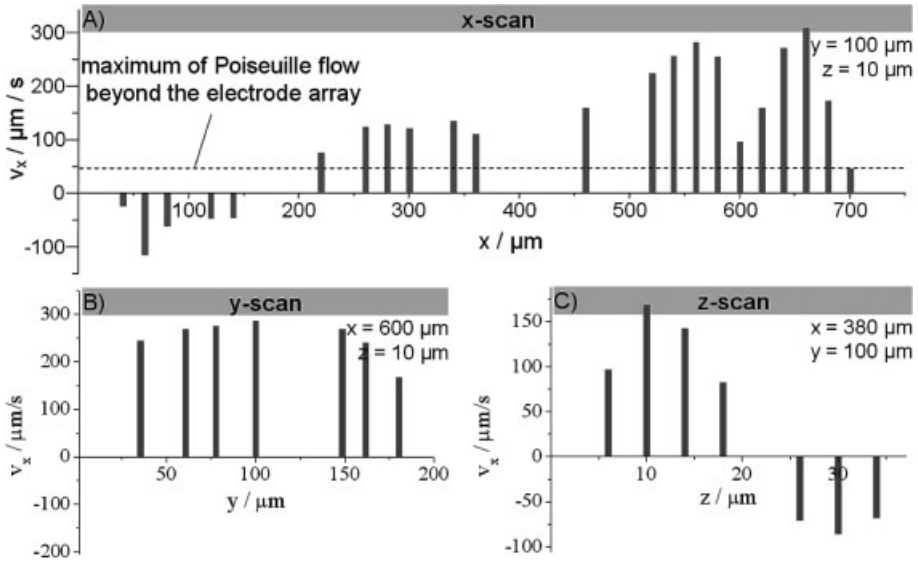


**Figure 5.** Flow velocities in *x*-direction measured with 2f-FCCS along three mutually perpendicular lines above the electrode array. While the flow outside the electrode array shows a laminar Poiseuille flow profile, the flow above the electrodes is less regular. A change in the flow direction can be found in the *x*-scan and in the *z*-scan. Negative signs indicate a flow opposite to the direction of the Poiseuille net flow, the maximum flow velocity of which is included in plot (A). The traveling wave pump was energized by electric signals of 8 V and 7 MHz.

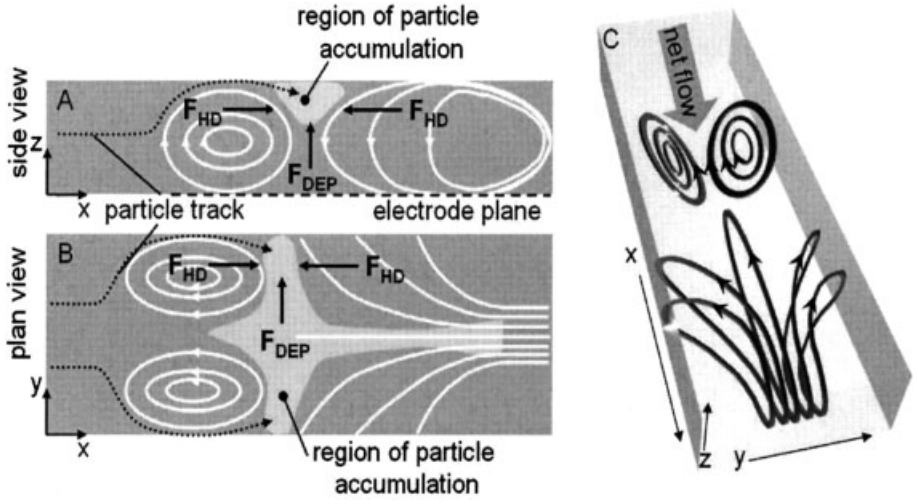


**Figure 6.** Scheme of the flow pattern as derived from visual particle tracking and from 2f-FCCS measurement and of the forces that act on the particles. The vortical streaming exerts hydrodynamic forces on the particles. These forces cause the motion of the particles away from the cores of the vortices. The particles move towards the regions between two adjacent vortices. Additionally, DEP forces act on the particles. They prevent the particles from approaching the channel bottom and push them from the channel center towards the sidewalls, where the electric field is lower.

summarizes the flow pattern obtained from the 2f-FCCS measurements together with the results of the visual particle tracking above the electrode array. The sketch shows a flow-line pattern that is consistent with our data. It features two vortices of different size rotating in opposite directions. In addition, the planes that are associated with closed flow lines are tilted in the case of the front vortex and bent in the case of the rear vortex. These peculiarities are a result of the visual tracking of particles.

### 3.3 Simulations

As these results are somewhat surprising – one would have expected the laminar flow to be predominant in such a geometry – the spatial distribution of the electric volume forces was investigated using finite element analysis. The distribution of the electric field as shown in Fig. 2C was determined by solving the Laplace equation [22]. The graph in Fig. 2D shows the field strength as a function of the *z*-coordinate along a line between two oppositely charged electrodes (*e.g.* between the first and second electrode from the left, Fig. 2C) where the field polarization is purely longitudinal. The Ohmic heating through the electric field determines the temperature field (Fig. 2A). It was calculated using the energy balance equation [25]. The temperature field determines the gradients of the electric conductivity and the dielectric constant [26]. Together with these gradients, the distribution of the vertical component of the electric field provides the input for the calculation of the polarization charges. The longitudinal component of the electric field times the polarization charge density then determines the electric force density $<f_{el}>$ that is responsible for the accel-

 

eration of the liquid in the *x*-direction [24]. Figure 2E depicts the mean force density averaged over one oscillation period as a function of *z*, the height above the electrode array. There is a maximum of the force density at a distance of 6 μm from the electrode array. More than 20 μm above the electrode array, the force value is only 10% of the maximum force density and only 16% of the overall force acts in this part of the channel. This confinement is a consequence of the electric field distribution and its various effects on the medium, namely the localized heating, the polarization of the medium through its vertical, and the "pulling" through its longitudinal, component.

## 4 Discussion

We observed complex flow behavior in our microchannels where fluidic transport is usually dominated by laminar flow lines. Propagating electric fields generated by arrays of microelectrodes act in a complex manner not only on the fluidic medium but also directly on the particles if they are bigger than 50 to 100 nm. For this reason, we applied 2f-FCCS to determine the flow profile, as it allows the introduction of probes that are not affected by the electric field, for example, through DEP interactions. These probes were 20 nm in diameter. Since the DEP force is proportional to the particle volume, they experienced an electric force, which was by more than one order of magnitude below that on the smallest particles, which exhibited accumulation. Hence, we are in the position to distinguish between forces that act on volume elements of the fluid medium and forces acting on particles. In addition to electric forces, thermal convection may also play a role, as the field distribution leads to localized Ohmic heating.

In the following, we first discuss the possible causes for the various features of the complex particle flow by elucidating how the force field determines the particle trajectories. Then, we focus on exploring whether the particle aggregation can be exploited for the filtering and sampling of nm- and μm-sized particles. Finally, we aim at improving the pumping.

The observation of the particle flow and the 2f-FCCS both provide evidence for the occurrence of two flow vortices above the electrodes. They rotate in opposite direction (Fig. 6). We first consider the causes that give rise to the vortex, which is closer to the rear end where the net flow leaves the array. We suppose that the combination of a localized force field above the electrode array and the flow resistance in the confined geometry of the microchannels is responsible for the rear vortex. Evidence for a localized force field is derived from the result of our calculation presented in Fig. 2. At the rear end of the array, the accelerated fluid elements experience a strong flow resistance. The flow evades into that part of the channel, where the electrohydrodynamic forces are too weak to counteract the flow resistance. Our 2f-FCCS data do not allow integrating the flow density over the entire cross-section of the channel. However, the higher positive flow velocities measured in the lower half of the microchannel close to the array are compatible with the positive net flow measured distant from the electrodes (Fig. 5C). A vertical component of the flow profile may be due to temperature convection. Its action might be most effective at the rear end of the array where the flow experiences a strong resistance.

At the front vortex, the flow profile as measured using 2f-FCCS contradicts the theoretical predictions. Which effects are neglected in our model calculations? First, heat convection and eventually liquid transport may affect the temperature distribution in this part of the microchannel. However, comparing the effectiveness of diffusive heat conduction with active transport based on the velocities observed and the dimensions of the channel shows that flow cannot compete with heat dissipation [24]. The effect of flow on the temperature pattern may at best smear out the temperature profile with respect to the calculations. To what extent heat convection plays a role in producing a more even temperature distribution in the chip is unclear. A second factor that may contribute to the observed behavior arises from the field distribution in front of the array boundary. The left triangle in Fig. 2C that indicates the direction of the force field in this part of the channel points opposite to the net flow. This is due to the orientation of the horizontal component of the electric field in this region as a result of the presence of the array boundary. It remains uncertain how far this contributes to the generation of the front vortex.

The ability to generate a well-defined vortical flow on a micrometer scale provides the possibility to manipulate nanosized particles through hydrodynamic forces. To explain the accumulation of particles, the behavior of a particle in a vortical flow is considered. When a particle is exposed to a vortex, radial forces act on the particle [27], *e.g.* centrifugal force, pressure gradient force, and Stokes drag. The crucial parameter determining whether the resulting radial force component points towards the center of the vortex or in the outward direction is the ratio between the liquid density $\rho_l$ and that of the particle $\rho_p$. For ratios $\rho_l / \rho_p < 1$, theory predicts the ejection of particles from the vortex center [28, 29], which was confirmed by several experimental investigations [30, 31]. In our case, $\rho_l / \rho_p = 0.95$. These results suggest that in our configuration particles should accumulate between the vortices. We observed enrichment in this region. However, the particles were confined to the channel wall opposite to the electrode array. This behavior is explained by DEP forces. Negative DEP acts on the particles such that the force vector points against the field gradient and particles are repelled away from the array towards the upper channel wall. As the strength of the DEP force is proportional to the volume of particles, the process of accumulation is more effective for larger particles than for smaller ones. This is what we observed.

 

Beyond this general behavior, we noticed more subtle effects when comparing the accumulation patterns for the 1-μm and the 200-nm particles. Hydrodynamic forces should be responsible for the enrichment of the particles in the center of the channel. The geometry of the vortices as proposed in Fig. 6 should lead to forces that point towards the center of the channel and induce particle accumulation in this region. In the case of the 1-μm particles, the center of the upper channel plane was free of particles, whereas the concentration of the 200-nm particles increased in this region. Obviously, DEP and hydrodynamic forces seem to act also along the *y*-axis. The focusing of the larger particles towards the sidewalls of the channel can be ascribed to negative DEP forces pushing the particles out from the channel center. For the smaller particles, DEP forces should be smaller by more than two orders of magnitude. The drag of fluid medium through the particles is not considered because of the low density of particles moving in the channel. This omission may be inapplicable in regions where particle agglomeration occurs.

How can the particle accumulation be optimized to design an effective filtering or enrichment device? A more complex design of the electrode arrays may offer various options for defining regions in the channel where enrichment or depletion of particles prevail. The arrangement of arrays in series or narrow arrays that are fabricated in parallel along the channel should offer possibilities for an efficient particle handling. This way, the positions of the vortices in the channels could be predefined. Narrow side channels that enter at positions where maximum particle density is achieved are considered as design elements that allow to continuously extract particles for producing concentrated particle suspension. Such an approach offers applications, *e.g.* in the detection of viruses in diluted samples for testing purposes. Today, this still is a complex and tedious task and could be accelerated using electrohydrodynamic particle aggregation. The sizes of the particles manipulated here were in the relevant range when compared to pathogenic viruses like influenza (110 nm) and smallpox (300 nm).

The formation of vortices reduces the efficiency of the electrohydrodynamic pumping. If one runs the device as a pump, the elimination or reduction of these vortices is desirable. What are the crucial parameters that determine the performance of the pump? The reduction of the channel dimensions should diminish the extent to which vortices occur as it enforces laminar flow. However, a reduced cross-section negatively affects the throughput. Shortening the length of the electrode array may also suppress the formation of vortices. A sequence of arrays in series may help suppress vortex formation. If one assumes that the occurrence of vortices depends on their size, then the spacing between the arrays could be a critical parameter. The electrode geometry, such as curved electrodes, modifies the boundaries and, therefore, may affect the vortices. To ascertain the most effective way of avoiding the vortices, more complex simulations together with variations of the design of the device are necessary.

Two advantages of the described method for particle trapping may be stressed. The first is the concomitant net pumping. Unfiltered suspension is continuously transported to the filtering element where the particles accumulate while the fluid moves on. The volume in which the accumulation actually occurs is strongly determined by the geometry of the vortices, hence, the effect is relatively long range. DEP, in contrast, only acts on those particles that happen to be within the field gradient in the vicinity of the microelectrodes. Filtering of a larger suspension volume is diffusion-limited or requires an additional pump. The second advantage lies in the mechanism, which is independent of interactions between particles, whereas pure DEP filtering of nanoparticles relies on sufficiently strong dipole attraction between particles. This requires a sufficient contrast in polarisability of the objects with respect to the medium and may exclude a number of interesting suspension from being processed by DEP. We expect that for a given particle concentration, filtering based on the traveling wave methods is significantly more effective than when using DEP alone.

We presented a microdevice that allows the generation of an electric traveling wave along a linear array of microelectrodes in a fluidic channel. Besides a possible exploitation for pumping small volumes of liquid media in microfluidic channels, in this work, we have also demonstrated that filtering and accumulation of micro- and nanoparticles from suspensions can be performed efficiently. We observed complex particle trajectories in the force field and the accumulation of particles in well-defined regions above the microelectrode array. By using 2f-FCCS, the velocity profile of only the fluid medium could be investigated. The forces that act directly on the particles were separated from those that act on the particles through the movement of the fluid. The analysis of the flow data indicates a flow pattern that consists of two vortices of different sizes and opposite directions of rotation. Particles accumulate preferentially between the vortices. Our results of finite element calculations identified a localized force field as one of the causes of the complex flow profile observed. In addition to the hydrodynamic forces, also DEP forces act on the particles and induce further particle focusing.

The electrode structures used can be integrated into a variety of channels. Through modified electrode geometries and the adjustable electric parameters, the orientation and strength of the forces can be adapted to applications like the detection of viruses, the structuring of surfaces with nanomaterials, or the purification of nanosuspensions.

*This work was supported by the German Research Foundation (DFG) in the framework of the Priority Program 1164 (JA 1717/1-2) and by the European Regional Development Fund (grant no. 4212/06-02).*

*The authors have declared no conflict of interest.*

 

## 5 References


[1] Salata, O. V., *J. Nanobiotech.* 2004, *2*, 3.

[2] Duschl, C., Geggier, P., Jaeger, M., Stelzle, M., in: Andersson, H., van den Berg, A. (Eds.), *Lab-on-chips for Cellomics: Micro- and Nanotechnologies for Life Science*, Kluwer Academic Publishers, Dordrecht, The Netherlands, 2004, pp. 83–122.

[3] Watarai, H., Namba, M., *Anal. Sci.* 2001, *17*, 1233.

[4] Wiklund, M., Toivonen, J., Tirri, M., Hanninen, P., Hertz, H. M., *J. Appl. Phys.* 2004, *96*, 1242–1248.

[5] Duerr, M., Kentsch, J., Mueller, T., Schnelle, T., Stelzle, M., *Electrophoresis* 2003, *24*, 722–731.

[6] Zhou, H., White, L. R., Tilton, R. D., *J. Colloid Interface Sci.* 2005, *285*, 179–191.

[7] Hoettges, K. F., Hughes, M. P., Cotton, A., Hopkins, N. A. E., McDonnell, M. B., *IEEE Eng. Med. Biol. Mag.* 2003, *22*, 68–74.

[8] Green, N. G., Morgan, H., *J. Phys. D: Appl. Phys.* 1998, *31*, L25–L30.

[9] Felten, M., Geggier, P., Jaeger, M., Duschl, C., *Phys. Fluids* 2006, *18*, 051707.

[10] Hagedorn, R., Fuhr, G., Mueller, T., Gimsa, J., *Electrophoresis* 1992, *13*, 49–54.

[11] Melcher, J. R., Firebaugh, M. S., *Phys. Fluids* 1967, *10*, 1178–1185.

[12] Elson, E. L., Magde, D., *Biopolymers* 1974, *13*, 1–27.

[13] Mets, U., Rigler, R., *J. Fluoresc.* 1994, *4(4)*, 259–264.

[14] Goesch, M., Blom, H., Holm, J., Heino, T., Rigler, R., *Anal. Chem.* 2000, *72*, 3260–3265.

[15] Kuricheti, K. K., Buschmann, V., Weston, K. D., *Appl. Spectrosc.* 2004, *58*, 1180–1186.

[16] Brister, P. C., Kuricheti, K. K., Buschmann, V., Weston, K. D., *Lab Chip* 2005, *5*, 785–791.

[17] Magde, D., Webb, W. W., Elson, E. L., *Biopolymers* 1978, *17*, 361–376.

[18] Koehler, R. H., Schwille, P., Webb, W. W., Hanson, M. R., *J. Cell Sci.* 2000, *113*, 3921–3930.

[19] Brinkmeier, M., Doerre, K., Stephan, J., Eigen, M., *Anal. Chem.* 1999, *71*, 609–616.

[20] Dittrich, P. S., Schwille, P., *Anal. Chem.* 2002, *74*, 4472–4479.

[21] Mueller, T., Gradl, G., Howitz, S., Schnelle, T., Fuhr, G., *Biosens. Bioelectron.* 1999, *14*, 247–256.

[22] Perch-Nielsen, I. R., Green, N. G., Wolff, A., *J. Phys. D: Appl. Phys.* 2004, *37*, 2323–2330.

[23] Stratton, J. A., *Electromagnetic Theory*, McGraw Hill, New York 1941.

[24] Ramos, A., Morgan, H., Green, N. G., Castellanos, A., *J. Phys. D: Appl. Phys.* 1998, *31*, 2338–2353.

[25] Schnelle, T., Mueller, T., Fuhr, G., *BioMethods* 1999, *10*, 417–452.

[26] Lide, D. R., *CRC Handbook of Chemistry and Physics*, CRC Press, Boca Raton, FL 2004.

[27] Raju, N., Meiburg, E., *Phys. Fluids* 1996, *9*, 299–314.

[28] Chein, R., Chung, J. N., *Int. J. Multiphase Flow* 1987, *13*, 785.

[29] Martin, J., Meiburg, E., *Phys. Fluids* 1994, *6*, 1116.

[30] Lazaro, B. J., Lasheras, J. C., *J. Fluid Mech.* 1992, *235*, 143.

[31] Lazaro, B. J., Lasheras, J. C., *J. Fluid Mech.* 1992, *235*, 179.


 